JGR Solid Earth

RESEARCH ARTICLE
10.1029/2020JB020076

Azimuthal Anisotropy of the Crust and Uppermost Mantle Beneath Alaska

L. Feng[1], Chuanming Liu[1], and M. H. Ritzwoller[1]

[1]Department of Physics, University of Colorado Boulder, Boulder, CO, USA

Key Points:
- An azimuthally anisotropic shear wave velocity model of Alaska is constructed from Rayleigh wave dispersion data
- Crustal anisotropy reflects the orientation of major faults across Alaska
- Mantle anisotropy is consistent with SKS splitting directions, revealing a toroidal pattern of fast directions around the Alaskan subduction zone

Correspondence to:
L. Feng,
lili.feng@colorado.edu

Citation:
Feng, L., Liu, C., & Ritzwoller, M. H. (2020). Azimuthal anisotropy of the crust and uppermost mantle beneath Alaska. *Journal of Geophysical Research: Solid Earth*, *125*, e2020JB020076. https://doi.org/10.1029/2020JB020076

Received 26 APR 2020
Accepted 25 OCT 2020
Accepted article online 30 OCT 2020

Abstract This study presents an azimuthally anisotropic shear wave velocity model of the crust and uppermost mantle beneath Alaska, based on Rayleigh wave phase speed observations from 10 to 80 s period recorded at more than 500 broadband stations. We test the hypothesis that a model composed of two homogeneous layers of anisotropy can explain these measurements. This "Two-Layer Model" confines azimuthal anisotropy to the brittle upper crust along with the uppermost mantle from the Moho to 200 km depth. This model passes the hypothesis test for most of the region of study, from which we draw two conclusions. (a) The data are consistent with crustal azimuthal anisotropy being dominantly controlled by deformationally aligned cracks and fractures in the upper crust undergoing brittle deformation. (b) The data are also consistent with the uppermost mantle beneath Alaska and surroundings experiencing vertically coherent deformation. The model resolves several prominent features. (1) In the upper crust, fast directions are principally aligned with the orientation of major faults. (2) In the upper mantle, fast directions are aligned with the compressional direction in compressional tectonic domains and with the tensional direction in tensional domains. (3) The mantle fast directions located near the Alaska-Aleutian subduction zone and the surrounding back-arc area form a toroidal pattern that is consistent with mantle flow directions predicted by recent geodynamical models. Finally, the mantle anisotropy is remarkably consistent with SKS fast directions, but to fit SKS split times, anisotropy must extend below 200 km depth across most of the study region.

1. Introduction

Alaska is part of a complex region, which includes a large subduction zone, the major rotational terrane of Arctic Alaska (e.g., Moore & Box, 2016), areas having undergone and continuing to undergo extensional tectonics (e.g., Johnston, 2001), and the successive accretion of terranes along both convergent and strike-slip fault zones (e.g., Coney & Jones, 1985; Johnston, 2001). The active Alaska-Aleutian subduction zone along the southern margin of Alaska is particularly complex, with ongoing subduction of the Pacific plate and collisional processes produced by the Yakutat microplate (e.g., Eberhart-Phillips et al., 2006). At present, different parts of Alaska continue to move relative to the stable North America plate, and significant seismicity is found across most of the state (e.g., Freymueller et al., 2008). The seismic data collected by the recently deployed EarthScope USArray Transportable Array (TA) and other local networks (Figure 1) provide the unprecedented opportunity to model and understand structures and dynamical processes beneath Alaska in much greater detail.

Previous seismic studies of the crust and mantle beneath Alaska have been based on a variety of types of data and techniques; however, most have focused on determining isotropic seismic structure (e.g., Jiang et al., 2018; Martin-Short et al., 2018; Ward & Lin, 2018). Studies of anisotropy have been based principally on shear wave splitting (e.g., Christensen & Abers, 2010; Hanna & Long, 2012; Venereau et al., 2019; Wiemer et al., 1999; Yang et al., 1995), although a few used surface waves (e.g., Feng & Ritzwoller, 2019; Wang & Tape, 2014) or body waves (e.g., Gou et al., 2019). Seismic anisotropy, in comparison with isotropic structure, is a second-order feature, and its observation is challenging. However, it is important because it can provide information about past and present-day deformation in the crust and mantle (e.g., Babuska & Cara, 1991; Crampin, 1984; Long, 2013; Long & Silver, 2008; Savage, 1999; Savage et al., 1990; Silver, 1996; Silver & Savage, 1994; Vinnik et al., 1992).

Among recent surface wave studies of anisotropy beneath Alaska, Feng and Ritzwoller (2019) present a 3-D model that includes apparent radial anisotropy of the shear wave speeds (V_{SV}, V_{SH}) in the crust and

Table 1
Names of the Structural Features Identified With Abbreviations in Figure 1

Abbreviation	Name
AA	Arctic Alaska
AT	Alexander Terrane
BR	Brooks Range
CC	Canadian Cordillera
DF	Denali Fault
KT	Koyukuk Terrane
NAC	North American Craton
TF	Tintina Fault
YCT	Yukon Composite Terrane
YT	Yakutat Terrane

uppermost mantle beneath Alaska. The inferred apparent crustal radial anisotropy is strongest across the parts of central and northern Alaska that were subject to large magnitude mid-Cretaceous extension. This is consistent with the crustal radial anisotropy being caused by deformationally oriented middle to lower crustal sheet silicates (micas) with shallowly dipping foliation planes beneath extensional domains (e.g., Hacker et al., 2014; Moschetti et al., 2010; Shapiro et al., 2004).

This paper complements the study of Feng and Ritzwoller (2019) by presenting a model of azimuthal anisotropy in the crust and uppermost mantle. The model is derived from the azimuthal variation of Rayleigh wave phase speed measurements from 10 to 80 s period observed at TA stations as well as other permanent and temporary networks in and around Alaska (Figure 1). In particular, we test the hypothesis that the data can be fit with a "two-layer" model in which azimuthal anisotropy is confined to the upper crust to a depth of 15 km and a single depth-invariant layer in the mantle from the Moho to a depth of 200 km.

Confining azimuthal anisotropy to the brittlely deforming upper crust is motivated by earlier studies in the mainland United States, Tibet, and Alaska (e.g., Feng & Ritzwoller, 2019; Lin et al., 2011; Moschetti et al., 2010; Shapiro et al., 2004; Xie et al., 2015, 2017). The single layer in the mantle is chosen for simplicity. We also test alternative models by confining the anisotropy to different depth ranges of the crust and the mantle. The tests indicate that the Rayleigh wave data prefer that mantle anisotropy extends from the Moho to the bottom of the model (200 km); however, we get similar data fitness from different crustal anisotropic models. Those alternate models are summarized and discussed in more detail in section 6 of the paper. We refer to the model we present here as the "Two-Layer Model."

Being able to fit the data with a single depth-invariant layer in the mantle is consistent with the vertical coherence of deformation in the mantle part of our model. By "vertically coherent deformation" we refer only to the mantle, as distinguished from the use of this term by Silver (1996), which refers to vertically coherent deformation in both the crust and the subcontinental mantle.

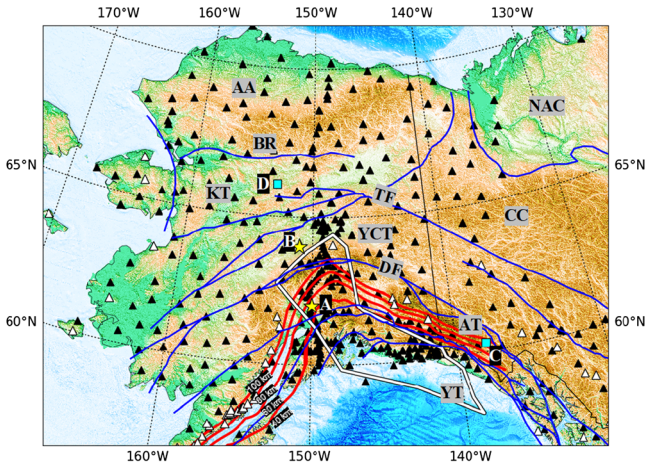

Figure 1. Seismic station distribution (black triangles) and volcanoes (white triangles) along with Blue lines = major faults, red lines = the top of the subducting Alaskan-Aleutian slab at depths of 40, 60, 80, and 100 km (Jadamec & Billen, 2010), and white polygon = the location of the hypothesized Yakutat Terrane (Eberhart-Phillips et al., 2006). Yellow stars are grid points located (A) south of Denali, north of the Cook Inlet and (B) north of Denali in the Yukon-Tanana terrane, referenced in Figures 2, 6a, and 6b. The cyan squares are locations used in Figures 6c and 6d, located in the (C) Alexander and (D) Koyukuk terranes where two mantle layers of anisotropy are needed to fit the data. Structural and tectonic features are identified with abbreviations explained in Table 1.

The principal novelty of this study lies in the construction of the first azimuthally anisotropic shear wave velocity model of the crust and uppermost mantle beneath Alaska, using Rayleigh waves extracted from both ambient noise and earthquakes. By measuring the azimuthally varying behavior of Rayleigh wave dispersion curves, we are able to constrain the crust and uppermost mantle azimuthal anisotropy simultaneously. Our study is similar in some respects to Wang and Tape (2014), who estimated the azimuthal behavior of Rayleigh waves based on earthquake data. However, there are three noteworthy differences. (1) We use both ambient noise and earthquake data to infer the azimuthal anisotropy. Introducing ambient noise data significantly improves the resolution at shallower depths, so that we can estimate crustal anisotropy. (2) We include data recorded through February 2019, which improves data coverage significantly, due to the widespread deployment of USArray TA after 2014. (3) Wang and Tape (2014) estimate azimuthally anisotropic phase speed maps at different Rayleigh wave periods, but we also infer an azimuthally anisotropic shear wave velocity model. As is shown later, the azimuthally anisotropic shear wave velocity model can be used to predict SKS splitting measurements, permitting comparison of Earth structures inferred from other observation (e.g., SKS splitting).

As discussed by Feng and Ritzwoller (2019), when inferring anisotropy using surface waves, it is useful to bear in mind two coordinate systems. The first is the frame defined by a symmetry axis (or foliation plane) of the medium of transport, in which "inherent" anisotropy is defined, and the second is the frame of the observations where "apparent" anisotropy

is observed. We follow Xie et al. (2017) and refer to measurements of anisotropy and inferences drawn from them in the observational frame as "apparent." Apparent shear wave azimuthal anisotropy refers to the dependence of propagation speed on azimuth. A common measure of the apparent shear wave azimuthal anisotropy is the fast azimuth φ_{SV} and amplitude A_{SV} of anisotropy, where the subscript "SV" means that anisotropy is in *V*sv. The fast azimuth φ_{SV} defines the direction in which the Rayleigh wave propagates with fastest speed and the anisotropy amplitude A_{SV} depicts the strength of the anisotropy in the fast azimuth direction.

Most studies of anisotropy, including this paper and the study of Feng and Ritzwoller (2019), report measurements and models of particular aspects of apparent anisotropy. In contrast, Xie et al. (2015, 2017) present methods that use observations of apparent radial and azimuthal anisotropy to infer characteristics of the depth-dependent elastic tensor as well as tilt information, which allows the inference of inherent anisotropy. The inference of inherent anisotropy is beyond the scope of this paper, however.

The paper is organized as follows. In section 2 we present information about the data sets and the tomographic method, including how we estimate uncertainties in the Rayleigh wave phase speed measurements and the quantities (e.g., A_{SV}, φ_{SV}) inferred from them. Section 3 presents examples of the 2-D Rayleigh wave azimuthally anisotropic phase speed maps along with corresponding uncertainties, and section 4 shows how the azimuthally anisotropic model is produced based on the first-order perturbation theory method of Montagner and Nataf (1986) to fit the azimuthal variation of dispersion data and uncertainties extracted from the tomographic maps. We present the features revealed by the model in section 5 and discuss them in section 6.

2. Data Set and Tomographic Method

2.1. Data

This study uses the Rayleigh wave phase speed dispersion measurements (10 to 80 s) produced by Feng and Ritzwoller (2019), which derive from both ambient noise cross correlation and earthquake waveforms. The seismic records are extracted from 22 permanent and temporary networks deployed across Alaska and northwest Canada between January 2001 and February 2019 (Figure 1), totaling 537 seismic stations. Feng and Ritzwoller (2019) provide more detailed information about the seismic arrays and data processing procedures.

2.2. Method

Based on measurements of Rayleigh wave phase time, we perform eikonal tomography (Lin et al., 2009), a geometrical ray theoretical method, to estimate local azimuthally dependent Rayleigh wave phase speed and associated uncertainty from ambient noise and earthquake dispersion data on a spatial grid with a spacing of about 20 km. To estimate the azimuthal variation of phase speed, we stack all phase speed versus azimuth measurements on a coarser spatial grid with a spacing of about 200 km and average the measurements in 18° azimuthal bins. As discussed further in section 6.1, the choice of 200 km for the "averaging radius" in which averaging occurs is ad hoc and affects the results, notably the amplitude of the inferred azimuthal anisotropy. However, averaging on this larger spatial grid improves the azimuthal coverage and reduces the scatter in the measurements but at the expense of degrading the spatial resolution. Figure 2 presents examples of the resulting azimuthal variation of phase speed for two sample grid points, Points A and B identified in Figure 1. For weakly anisotropic media, the azimuthally binned Rayleigh wave phase speed measurements can be fit with a sinusoidal function (Smith & Dahlen, 1973), which indicates the 2-ψ azimuthal variation:

$$C(\omega,\psi) = C_{\mathrm{iso}}(\omega)\{1 + A(\omega)\cos[2(\psi - \varphi_{\mathrm{FA}}(\omega))]\} \quad (1)$$

where ψ is the azimuth, ω is the angular frequency, C_{iso} is the isotropic phase speed, $\varphi_{\mathrm{FA}}(\omega)$ is the fast azimuth of 2-ψ anisotropy, and $A(\omega)$ is the amplitude of 2-ψ anisotropy. Estimates of $\varphi_{\mathrm{FA}}(\omega)$ and $A(\omega)$ with corresponding uncertainties, computed by error propagation from the measured to inferred quantities, are notated on the panels of Figure 2.

Lin and Ritzwoller (2011) reported that a 1-ψ pattern in the phase speed measurements can be observed for long-period surface waves near strong isotropic structural gradients caused by backscattering in

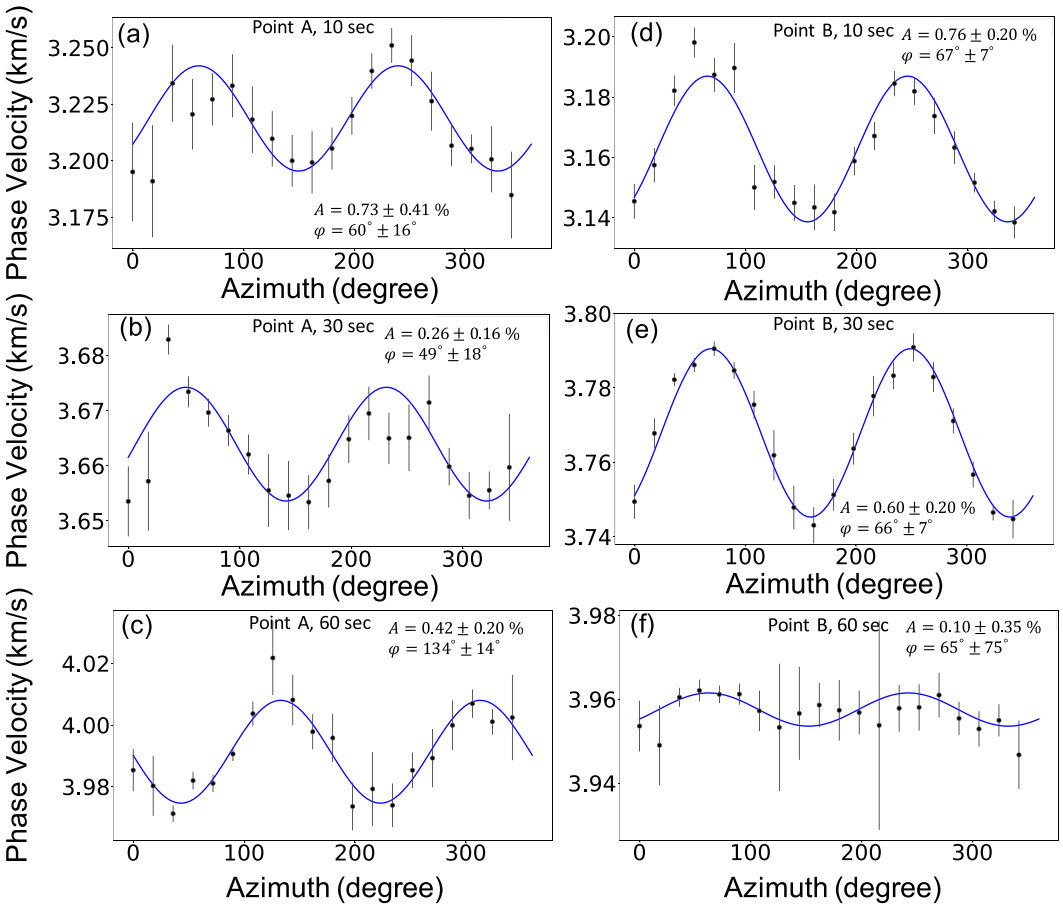

Figure 2. Azimuthal bin-averaged phase velocity measurements (black dots) and bin standard deviations (error bars) at periods of 10, 30, and 60 s plotted versus azimuth (ψ) measured using the eikonal tomography method at Locations A and B identified in Figure 1. (a–c) Point A; (d–f) Point B.

heterogeneous isotropic media. This effect may contaminate estimates of $\varphi_{\mathrm{FA}}(\omega)$ and $A(\omega)$, particularly at long periods (>50 s). This is because backscattering, which is essentially a finite frequency effect, is typically stronger at longer periods. Because we also observe strong 1-ψ patterns at long periods in some places, we simultaneously estimate the 1-ψ and 2-ψ components, as suggested by Lin and Ritzwoller (2011), but report only the 2ψ component. A full parametric form of the azimuthal anisotropy of both Rayleigh and Love waves should include a 4ψ term (Smith & Dahlen, 1973). In this study, however, we ignore the 4-ψ term because it is typically very weak for Rayleigh waves (e.g., Montagner & Nataf, 1986).

The reliability of the estimates of 2-ψ azimuthal anisotropy can be assessed by comparing estimates of $\varphi_{\mathrm{FA}}(\omega)$ and $A(\omega)$ determined separately from the ambient noise and the earthquake data sets in the period band of overlap. In Figure 3, we compare the azimuthal anisotropy maps at 30 s period from ambient noise tomography (ANT) and earthquake tomography (ET). The fast azimuths yielded by ANT and ET are largely consistent (Figures 3a and 3b). Indeed, Figure 3c shows the angle differences in fast azimuth, and the corresponding histogram (Figure 3d) indicates that at more than 80% of the locations there is an angle difference smaller than 30°. Large differences in fast azimuth are located in the northern and southern parts of the study region, where the strength of anisotropy is weaker and azimuthal coverage is less complete and, therefore, the fast azimuth is less well constrained. A comparison with similar results was performed for the western United States by Lin et al. (2011), in which the authors showed the consistency in azimuthal anisotropy determined separately by ambient noise and earthquake data with results that are similar to those reported here.

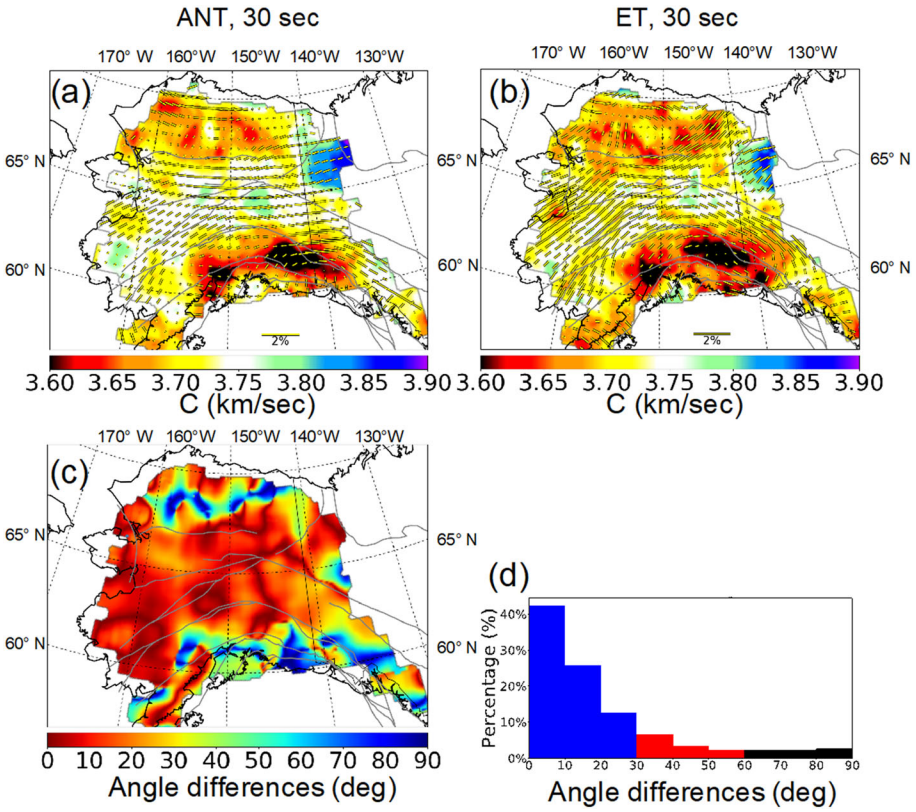

Figure 3. (a) Rayleigh wave phase speed at a period of 30 s along with the amplitude and fast-axis directions for azimuthal anisotropy constructed with ambient noise tomography (ANT). (b) Similar to (a), but constructed by earthquake tomography (ET). (c) The fast-axis angle differences between ANT and ET. Large differences in fast azimuth are located in the northern and southern parts of the study region, where the strength of anisotropy is weaker and azimuthal coverage is less complete. (d) Corresponding histogram of (c). More than 80% of the data points have an angular difference less than 30°.

Final maps of fast axis, $\varphi_{FA}(\omega)$, and anisotropy amplitude, $A(\omega)$, combine the measurements from ambient noise and earthquakes rather than performing tomography for each data set separately. At periods from 10–18 s, there are only ambient noise measurements, but from 20–60 s the measurements are combined from ambient noise and earthquakes. We consider the measurements from ambient noise and earthquakes to be equally reliable and do not down-weight either of the data sets as long as the results pass the quality control scheme. The quality control scheme includes the following measures: (1) discarding dispersion measurements with SNR < 15, (2) checking the phase travel time curvature, and (3) requiring at least four nearby stations located east/west/north/south, respectively, from each grid point such that the spatial gradient computation is accurate. At >50 s, earthquake results dominate the finalized phase speed maps because there are more measurements that pass the quality control for earthquakes. For periods above 60 s, there are only earthquake measurements. Weights applied to the two data sets upon combination at different periods are based on the relative signal-to-noise ratios of ambient noise and earthquake data. The combination of the two types of measurements (ambient noise and earthquake travel times) significantly improves the azimuthal coverage of the phase speed measurements and thus enhances the quality of the estimates of azimuthal anisotropy. Examples of the final phase velocity maps are presented with azimuth- and amplitude-dependent bars at periods of 10, 30, 60, and 80 s in Figure 4.

We estimate uncertainties in the azimuthal dependence of the phase speed measurements by taking the standard deviation of the mean in each azimuthal bin at each location and period. Uncertainties in $\varphi_{FA}(\omega)$ and $A(\omega)$ are derived values, estimated by error propagation in the regression for these quantities from the azimuthally dependent measurements. Lin et al. (2009) argue that the uncertainties in isotropic phase speeds are underestimated because this procedure does not account for systematic errors or the

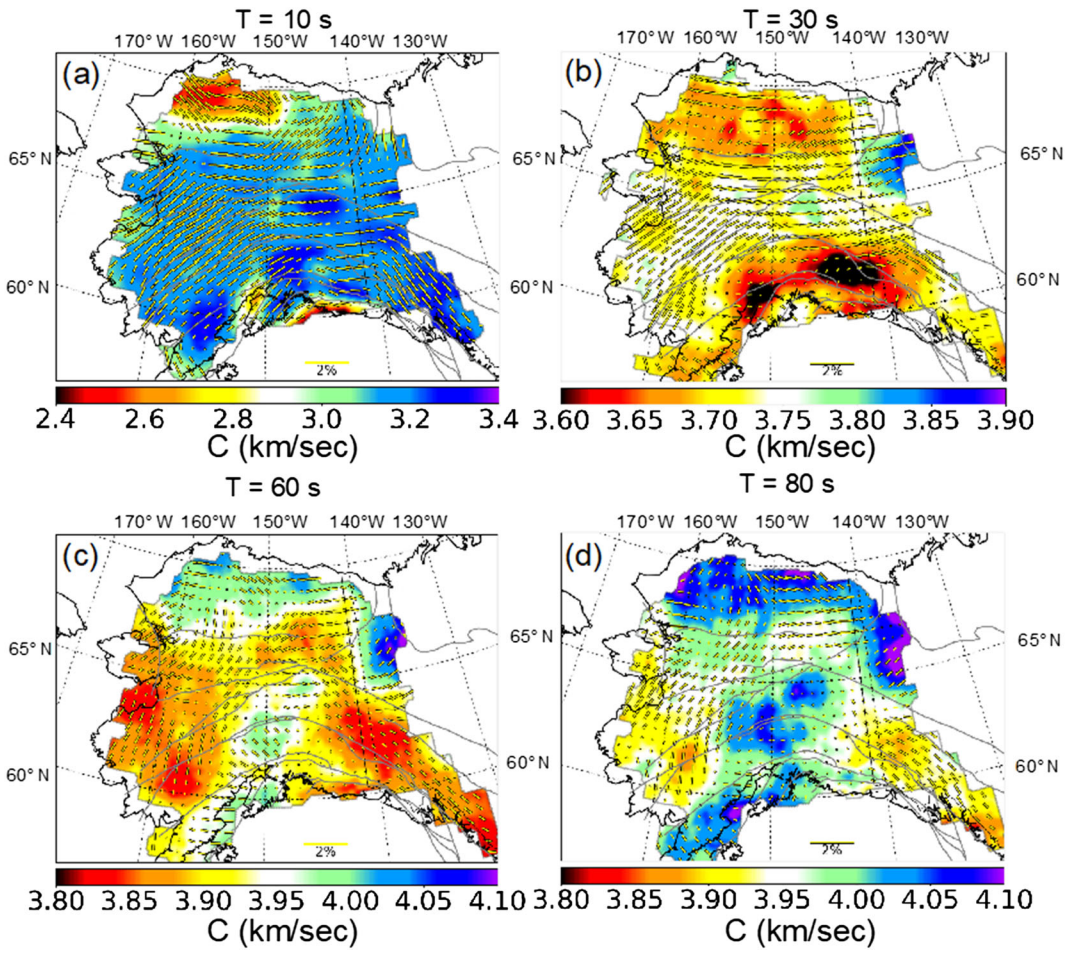

Figure 4. Example Rayleigh wave azimuthal anisotropy maps superimposed on isotropic phase speed for the final data set constructed from a combination of ambient noise and earthquake measurements at periods of (a) 10 s, (b) 30 s, (c) 60 s, and (d) 80 s.

correlation of errors for different measurements at different periods. We agree that uncertainties in $\varphi_{\mathrm{FA}}(\omega)$ and $A(\omega)$ are probably underestimated, so we scale up uncertainties in each quantity so that about two thirds (~68%) of the uncertainty values are larger than the differences between ambient noise and earthquake based estimates of $\varphi_{\mathrm{FA}}(\omega)$ and $A(\omega)$ across the region of study. This is justified by assuming the data sets satisfy random Gaussian distributions and the uncertainty should be one standard deviation of the Gaussian distribution. We scale up the uncertainty in fast azimuth, $\varphi_{\mathrm{FA}}(\omega)$, by a factor of 3.5 and the uncertainty in amplitude, $A(\omega)$, by a factor of 4.0. The upscaled values are reflected in the uncertainty maps shown in Figure 5 and in other subsequent figures.

3. Rayleigh Wave Azimuthal Anisotropy Results

Rayleigh waves at different periods are sensitive to different depths within the Earth. Therefore, the period-dependent dispersion information, in both amplitude and azimuth dependence, can help to infer azimuthal anisotropy in different depth ranges. Indeed, between 10 and 30 s period, where Rayleigh waves are primarily sensitive to the Earth's crust in continental areas, the patterns of the fast directions of azimuthal anisotropy are similar to one another in the interior of Alaska. Figures 4a and 4b present examples at 10 and 30 s period. Fast directions run nearly parallel to the principal local orientation of major faults, which may result from the generation of crustal azimuthal anisotropy from deformationally oriented cracks and fractures. In contrast, at 60 s period (Figure 4c), which is more sensitive to mantle depths, we observe that

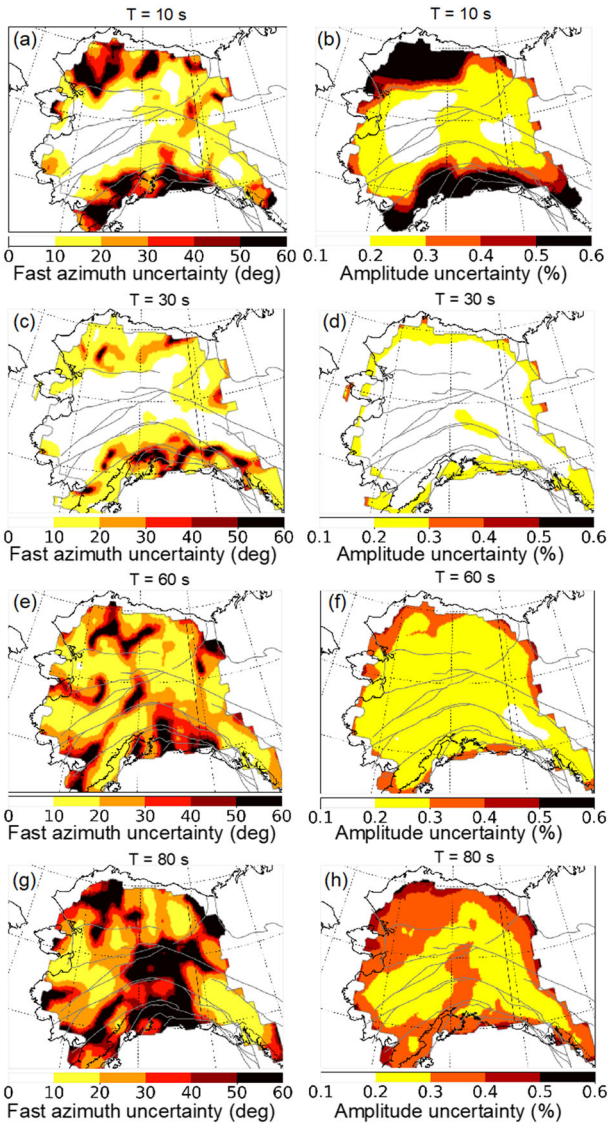

Figure 5. Example maps of one standard deviation uncertainty estimates in fast azimuth (left) and anisotropy amplitude (right) at periods of (a, b) 10 s, (c, d) 30 s, (e, f) 60 s, and (g, h) 80 s.

the fast directions within the subducting slab region (i.e., radially above the subducting slab) are mostly perpendicular to the northwestern slab edge in map view. We cannot resolve whether this anisotropy is produced within the slab, above the slab, below the slab, or in all three depth zones. Prevailing opinion is that the strongest anisotropy in subduction zones exists in the mantle wedge (e.g., Behn et al., 2007; Long & van der Hilst, 2006), but other studies point out that it may come from beneath the slab (e.g., Long & Silver, 2008) or in the slab (e.g., Faccenda et al., 2008). Whatever depth the anisotropy derives from, the fast orientations shift to slab edge-parallel patterns in the back-arc region. This as a whole constructs a large-scale rotational pattern in the fast-axis distribution, apparently related to the subducting Pacific slab. Together with the high-speed slab anomaly, this rotational pattern moves northward at 80 s period (Figure 4d). Patterns of fast directions similar to this have been reported by previous studies of SKS splitting (e.g., Christensen & Abers, 2010; Hanna & Long, 2012; Venereau et al., 2019).

It is instructive to compare our azimuthally anisotropic phase speed maps with those maps presented by Wang and Tape (2014) at similar periods, namely, our 30 and 60 s maps with the 33 and 59 s maps from Wang and Tape (2014). At ~30 s period, the Rayleigh wave is mostly sensitive to crustal structures. The fast axes in our 30 s map (Figure 4b) are largely oriented along major faults, while the 33 s map from Wang and Tape (2014) does not show this fault-related pattern. The 60 s map (Figure 4c) in our study shows a toroidal pattern in fast directions that is related to the slab; the pattern is not as clear in the 59 s map presented by Wang and Tape (2014). We believe that these differences arise due to the improved resolution in the phase speed maps caused by a greater number of measurements. In addition, we apply eikonal tomography to produce the azimuthally anisotropic phase speed maps, which is different from conventional methods (e.g., Petrescu et al., 2017; Wang & Tape, 2014). One of the important advantages of eikonal tomography is that the results (particularly the fast-axis directions, as dicussed further in section 6.1) are less dependent on the choice of subjective regularization parameters. Eikonal tomography more directly yields sinusoidal azimuthally varying patterns from the measurements (e.g., Figure 2).

Examples of estimates of uncertainties (appropriately upscaled) in fast azimuth and the amplitude of anisotropy are presented in Figure 5. Uncertainties are smallest at 30 s period because high quality data from both ambient noise and earthquakes exist at this period, similar to uncertainties in isotropic shear wave speeds (Feng & Ritzwoller, 2019). Uncertainties in fast azimuth estimates maximize locally where anisotropy amplitudes are smallest.

From the Rayleigh wave azimuthal anisotropy maps constructed from both ambient noise and earthquake data sets, we extract local azimuthal anisotropy dispersion curves on a 20-km grid across the study region. To improve the robustness of the results, we stack results from all nearby points on a 200 km grid. This reduces the resolution of anisotropy to about 200 km and also affects the amplitude of the resulting maps, as discussed further in section 6.1. The resulting azimuthally dependent curves are the basis for the inversion for shear wave azimuthal anisotropy in the two layers of the crust and mantle. Example azimuthal anisotropy dispersion curves along with corresponding uncertainties for the Sample Points A–D, identified in Figure 1, are shown in Figure 6. The period dependence of these curves provides the depth resolution, with crustal anisotropy dominantly constrained by measurements below about 30 s period and mantle anisotropy determined by the longer-period measurements.

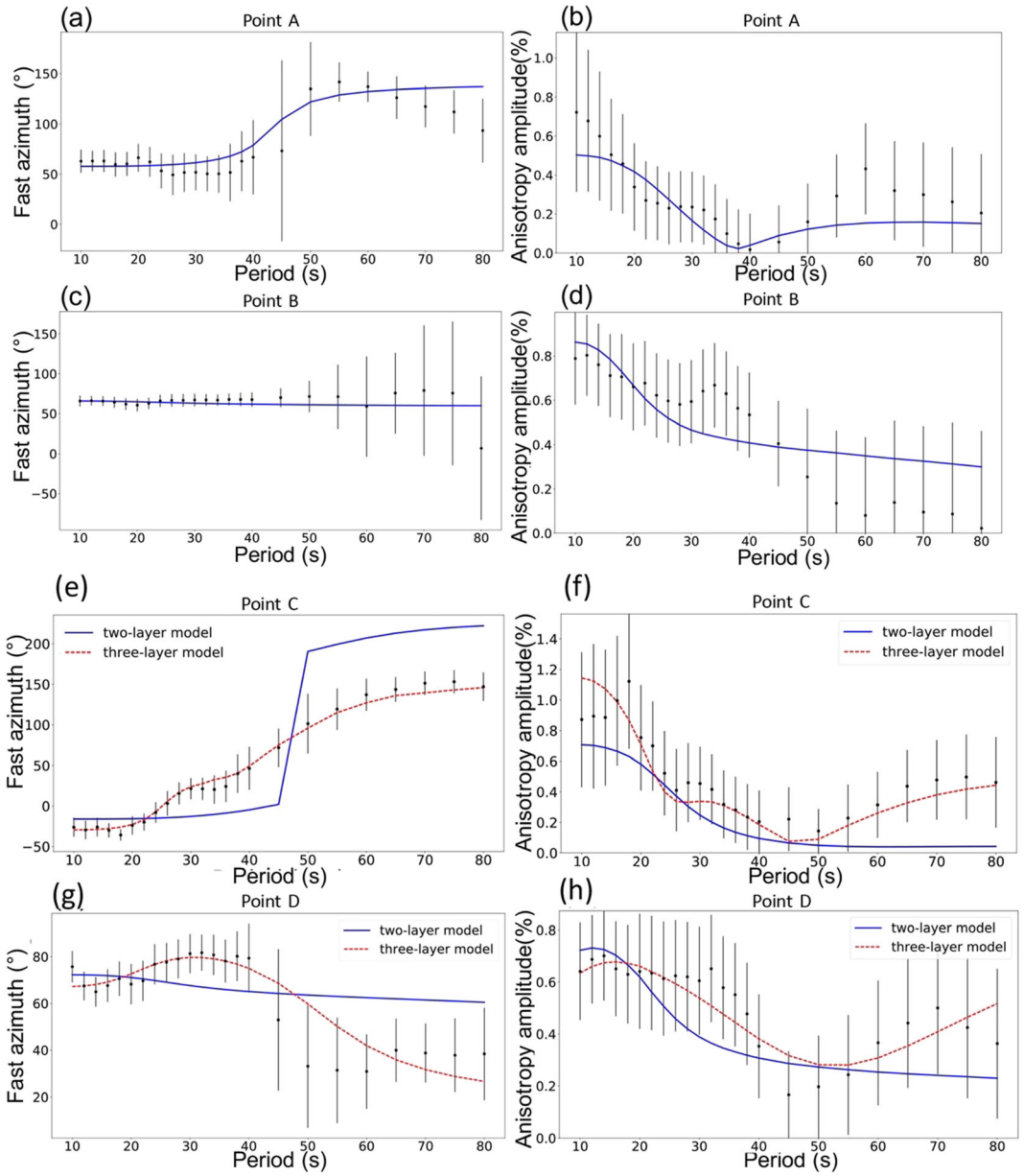

Figure 6. Anisotropy dispersion curves of fast azimuth, $\phi_{FA}(\omega)$, and amplitude, $A(\omega)$, for the Sample Points A–D identified in Figure 1. One standard deviation error bars are observed data, the blue lines are predictions from the Two-Layer Model of azimuthal anisotropy, and red lines are predictions from the Three-Layer Model where two anisotropic mantle layers are included. At Points A and B the Two-Layer Model fits the data, but at C and D a second mantle layer must be added to fit the data. (a, b) Point A. (c, d) Point B. (e, f) Point C. (g, h) Point D.

4. Inversion Procedure

In this section, we present the model parameterization and inversion method, namely, how we infer the two-layer azimuthal anisotropy model based on the Rayleigh wave azimuthally anisotropic maps at different periods.

4.1. Model Parameterization

As discussed in section 1, the inversion tests the hypothesis that azimuthal anisotropy is principally confined to two vertically homogeneous layers: the upper crust from the base of the sediments to a depth of 15 km and the mantle from the Moho to 200 km depth. Under this hypothesis, crustal anisotropy at depths less than

15 km is produced primarily by brittle deformation, which generates oriented cracks and fractures at multiple length scales (e.g., Crampin, 1984). Confining azimuthal anisotropy to the brittlely deforming upper crust is motivated by earlier studies in the United States, Tibet, and Alaska (e.g., Feng & Ritzwoller, 2019; Moschetti et al., 2010; Shapiro et al., 2004; Xie et al., 2015, 2017). Those studies provided evidence of strong radial anisotropy in the lower crust. Assuming that crustal material is intrinsically tilted transversely isotropic (TTI), a vertically oriented symmetry axis would produce strong radial anisotropy and weak azimuthal anisotropy. Mantle azimuthal anisotropy may also be strong, being caused by the lattice-preferred orientation (LPO) of olivine, associated with large-scale deformation and mantle flow. For simplicity, we parameterize mantle azimuthal anisotropy as vertically homogeneous (single layer) at each location, and this still allows the data to be fit across most of the study region.

We do not include azimuthal anisotropy in the sediments or in the lower crust, where we hypothesize that azimuthal anisotropy is relatively weak across the region of study and anisotropy is largely radial at these depths. Thus, we parametrize the Two-Layer Model with two independent anisotropic layers with depth-independent anisotropy in each. We acknowledge that the hypothesis in which azimuthal anisotropy is confined in the upper crust is not uniquely supported by the data, so this should be considered an open question requiring more research. Indeed, as discussed later in section 6.2, we get similar data fitness by confining the azimuthal anisotropy to different depth ranges of the crust as a single anisotropic layer. Future work of introducing additional data sets (e.g., receiver functions and shear wave splitting) and performing the inversion as depth-dependent elastic tensor by interpreting Rayleigh wave azimuthal anisotropy simultaneously with Love wave data (e.g. Xie et al., 2015) would further test this hypothesis.

The inferred model comprises two pairs of anisotropy values at each location, fast azimuth φ_{SV} and anisotropy amplitude A_{SV}: namely, $\left(\varphi_{SV}^{(1)}, A_{SV}^{(1)}\right)$ in the upper crust and $\left(\varphi_{SV}^{(2)}, A_{SV}^{(2)}\right)$ in the mantle. The symbols φ_{SV} and A_{SV} are depth-dependent quantities that differ from the symbols for frequency-dependent fast azimuth and anisotropy amplitude of Rayleigh waves, namely $\varphi_{FA}(\omega)$ and $A(\omega)$. The $\varphi_{FA}(\omega)$ and A(ω) and associated uncertainties are the inputs for the inversion, while $\left(\varphi_{SV}^{(1)}, A_{SV}^{(1)}\right)$ and $\left(\varphi_{SV}^{(2)}, A_{SV}^{(2)}\right)$ and uncertainties are the outputs. $\left(\varphi_{SV}^{(2)}, A_{SV}^{(2)}\right)$.

4.2. Inversion Scheme

The inversion scheme is similar to that used in the studies of Yao et al. (2010) and Lin et al. (2011). It is based on the first-order perturbation theory presented by Montagner and Nataf (1986), which describes the azimuthal variation of Rayleigh wave phase speed, C_R, as

$$\delta C_R(\omega,\psi) = \int_0^H \left\{ \left((B_c \cos 2\psi + B_s \sin 2\psi) \frac{\partial C_R}{\partial A}\bigg|_0 + (G_c \cos 2\psi + G_s \sin 2\psi) \frac{\partial C_R}{\partial L}\bigg|_0 + (H_c \cos 2\psi + H_s \sin 2\psi) \frac{\partial C_R}{\partial F}\bigg|_0 \right\} dz \right. \tag{2}$$

In Equation 2, B_c, B_s, G_c, G_s, H_c, and H_s are linear combinations of the components of the azimuthally variable parts of the elastic modulus matrix, and $\frac{\partial C_R}{\partial A}|0$, $\frac{\partial C_R}{\partial L}|0$, and $\frac{\partial C_R}{\partial F}|0$ are the sensitivity kernels for three of the five elastic parameters ($A = \rho V_{PH}^2$, $C = \rho V_{PV}^2$, $N = \rho V_{SH}^2$, $L = \rho V_{PV}^2$, and F) that describe transversely isotropic (TI) media.

In the end, we omit the H_c and H_s terms, which provide sensitivity to the elastic modulus F, because their impact on Rayleigh wave phase speed is believed to be small based on empirical mineralogical models (Montagner & Nataf, 1986). Based on studies of olivine (Montagner & Nataf, 1986) as well as mica and amphibole in crustal rocks (Barruol & Kern, 1996), we assume that $B_{c,s}/A = G_{c,s}/L$, like Lin et al. (2011). Thus, Equation 2 can be simplified as

$$\delta C_R(\omega,\psi) = \int_0^H \left\{ G_c \cos 2\psi \left(\frac{A}{L}\frac{\partial C_R}{\partial A}\bigg|_0 + \frac{\partial C_R}{\partial L}\bigg|_0 \right) + G_s \sin 2\psi \left(\frac{A}{L}\frac{\partial C_R}{\partial A}\bigg|_0 + \frac{\partial C_R}{\partial L}\bigg|_0 \right) \right\} dz \tag{3}$$

Given the transversely isotopic reference velocity model constructed by Feng and Ritzwoller (2019), we use a TI forward code (Herrmann, 2013) with Earth flattening to compute the depth-dependent sensitivity kernels

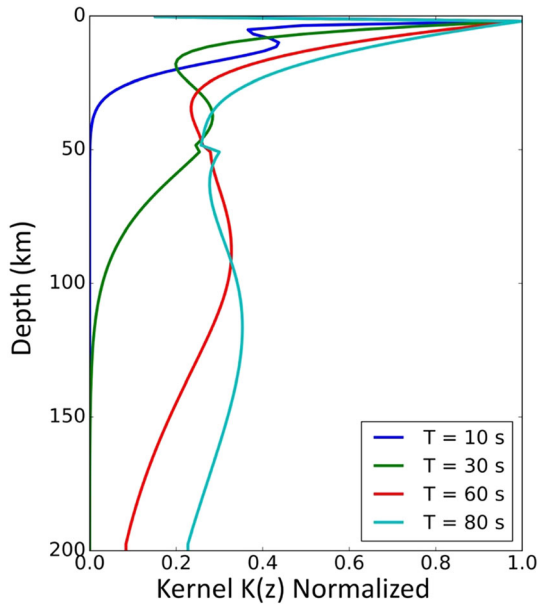

Figure 7. Examples of the integrals kernels, $K(z)$, from Equation 3 at periods of 10, 30, 60, and 80 s. Kernels are normalized by their maximum amplitude so that each normalized kernel has an amplitude of unity. The peak amplitudes of the nonnormalized kernels decrease with period. Not shown here: The sensitivity kernels are more sensitive to azimuthal anisotropy in V_{PH} in the shallow crust and V_{SV} in the mantle.

for the moduli A and L (e.g., Xie et al., 2015). The resulting sensitivity kernel, which we refer to as $K(z)$ for the effective moduli G_c (or G_s) is $K(z) = (A/L)\partial C_R/\partial A + \partial C_R/\partial L$. Because the modulus A is related to V_{PH} and L is related to V_{SV}, $K(z)$ is sensitive to anisotropy in both compressional and shear wave speeds. Amplitude normalized examples of $K(z)$ at four periods are presented in Figure 7. The shallower part of the kernel is more sensitive to V_{PH}, and the deeper parts are more sensitive to V_{SV}. Thus, the data we use are more sensitive to azimuthal anisotropy in V_{PH} in the crust and V_{SV} in the mantle.

We use the observed azimuthal anisotropy dispersion curves of $\varphi_{FA}(\omega)$ and $A(\omega)$ (e.g., Figure 6) to estimate simultaneously $\left(G_c^{(1)}, G_s^{(1)}\right)$ and $\left(G_c^{(2)}, G_s^{(2)}\right)$ in the upper crust and mantle, respectively, by linear inversion. Similar to Yao et al. (2010), the fast azimuth φ_{SV} and anisotropy amplitude A_{SV} are determined from the moduli G_c and G_s as follows for the upper crust and mantle:

$$\varphi_{SV} = \frac{1}{2}\tan^{-1}\left(\frac{G_s}{G_c}\right) \tag{4}$$

and

$$A_{SV} = \frac{1}{2L}\sqrt{G_c^2 + G_s^2} \tag{5}$$

Corresponding uncertainties are determined from the estimated model covariance matrix (Tarantola, 2005).

The result is a two-layer azimuthally anisotropic model which reflects the distribution of azimuthal anisotropy in the upper crust and uppermost mantle. We describe the results of the inversion in section 5 and discuss them in section 6.

5. Results of the Inversion

The inversion results in a two-layer model, namely, $\left(\varphi_{SV}^{(1)}, A_{SV}^{(1)}\right)$ in the upper crust to 15 km depth and $\left(\varphi_{SV}^{(2)}, A_{SV}^{(2)}\right)$ in the mantle to 200 km depth, as shown in Figure 8. Consistent with the shorter-period Rayleigh wave observations, the upper crustal fast directions are principally aligned with the major faults, as discussed further in section 6.2. In contrast, the distribution of mantle fast directions is similar to the longer-period observations and results in a different pattern that is discussed further in section 6.3.

The average amplitude of crustal anisotropy is stronger in the crust than in the mantle, averaging 1.3% in the crust and 0.4% in the mantle. Uncertainty in the fast directions maximize where the amplitudes of anisotropy minimize. The uncertainty also tends to be larger near the periphery of the region of study where azimuthal coverage degrades. For this reason, the fast-axis uncertainty is not particularly informative abstracted from the amplitude of anisotropy, but we note that the one standard deviation uncertainty for fast axes averages about 8° in the crust across the region of study and about 13° in the mantle. The one standard deviation uncertainty for the amplitude of azimuthal anisotropy averages about one-half the average amplitude across the region of study: 0.7% for the crust and 0.2% for the mantle. As discussed in section 6.1, however, the amplitude of anisotropy is particularly affected by the choice of the averaging radius applied to the measurements. As a result, amplitudes may be biased low in a way that is not captured by the error statistics.

We are interested in testing the null hypothesis that the Two-Layer Model can fit the data acceptably and as well as more complicated distributions of anisotropy in the crust and mantle. Misfits to observations of fast azimuth and anisotropy amplitude by predictions from the resulting two-layer model are shown in Figure 9. We define the misfit as follows:

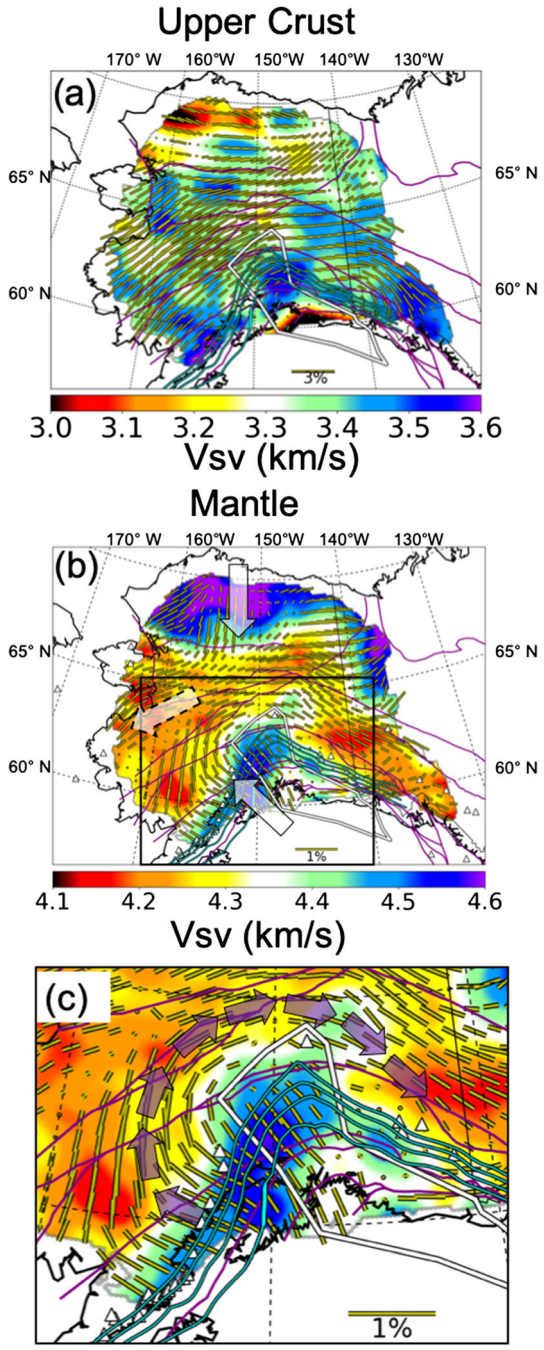

Figure 8. Two-Layer Model of azimuthal anisotropy. (a) Upper crustal azimuthal anisotropy; the background color indicates average *V*sv in the depth range. (b) Mantle azimuthal anisotropy from Moho to 200 km depth; the background color indicates *V*sv at 100 km depth. Faults, the hypothesized Yakutat terrane, and the top slab edges from 40 to 100 km depth are as in Figure 1. The two arrows in the north and south show the compressional deformation direction of the Arctic Alaska Terrane and the Alaskan subduction zone, while the dashed arrow in the interior region shows the "escaping" direction of interior Alaska, which represents the tensional deformation direction. The rectangular box identifies the region that is zoomed in. (c) A zoom-in to the subduction zone to better illustrate the toroidal flow pattern, as indicated by the overlaying purple arrows.

$$\chi = \sqrt{\frac{1}{N}\sum_{i=1}^{N}\frac{(\Delta d_i)^2}{\sigma_i^2}} \tag{6}$$

where Δd_i is the difference between an observed datum (fast azimuth or anisotropy amplitude) and the value predicted by the model, and σ_i is the one standard deviation data uncertainty. The index i ranges over period at a location for $\varphi_{\mathrm{FA}}(\omega)$ and $A(\omega)\varphi_{\mathrm{FA}}(\omega)$, where N is the number of the data values or periods. Δd_i for fast azimuth is defined as

$$\Delta d_i = \begin{cases} \left|\varphi_i^{obs} - \varphi_i^{pre}\right|, & if\ \left|\varphi_i^{obs} - \varphi_i^{pre}\right| \le 90° \\ 180° - \left|\varphi_i^{obs} - \varphi_i^{pre}\right|, & if\ \left|\varphi_i^{obs} - \varphi_i^{pre}\right| > 90° \end{cases} \tag{7}$$

where φ_i^{obs} is the observed fast azimuth and φ_i^{pre} represents the predicted value. For anisotropy amplitude, Δd_i is defined as follows:

$$\Delta d_i = A_i^{obs} - A_i^{pre} \tag{8}$$

where A_i^{obs} is the observed anisotropy amplitude and A_i^{pre} indicates the predicted value. Assuming the Δd_i satisfies a Gaussian distribution with standard deviation of σ_i, the expected value of misfit χ would be 1. Therefore, we consider misfit values below 1 as acceptable. Figure 9 indicates that for most parts of the study region acceptable values in misfit are found.

The Two-Layer Model with azimuthal anisotropy confined to the uppermost crust and to a single layer in the mantle can fit the amplitude of Rayleigh wave anisotropy across essentially the entire region of study (Figure 9b) and predict the Rayleigh wave fast azimuth directions across most of the region of study (Figure 9a). Thus, for the amplitude of azimuthal anisotropy the null hypothesis is supported; no model of anisotropy more complicated than the Two-Layer Model is needed to fit observations of the amplitude of azimuthal anisotropy. Misfit in fast azimuth (Figure 9a) is substantial only in the Alexander and Koyukuk terranes (identified as AT and KT in Figure 1). In fact, as shown in Figures 9c and 9d, fast azimuth misfit is confined principally to periods above 40 s, consistent with the need to add a second mantle layer in these two terranes. Therefore, the null hypothesis is supported for the fast azimuth of anisotropy across most of Alaska but is rejected in the Alexander and Koyukuk terranes where an additional mantle layer is required to fit the data, as discussed further in section 6.3.6.

6. Discussion

6.1. Effect of the Averaging Radius on Amplitude and Fast Axis of Anisotropy

In section 2.2 we discuss how the measurements of phase times are averaged in 200 km radius geographic bins as a function of azimuth to produce the estimates of azimuthal anisotropy. The choice of 200 km as the averaging radius is ad hoc. Larger values reduce the scatter in the measurements but at the expense of reducing resolution and the amplitude of anisotropy. This effect is illustrated in Figure 10a at 40 s period for two averaging radii (blue error bars: 120 km, red error bars: 200 km) for a single location (−156W, 63N). The choice of the larger averaging radius reduces the incidence of outliers and reduces the amplitude of the

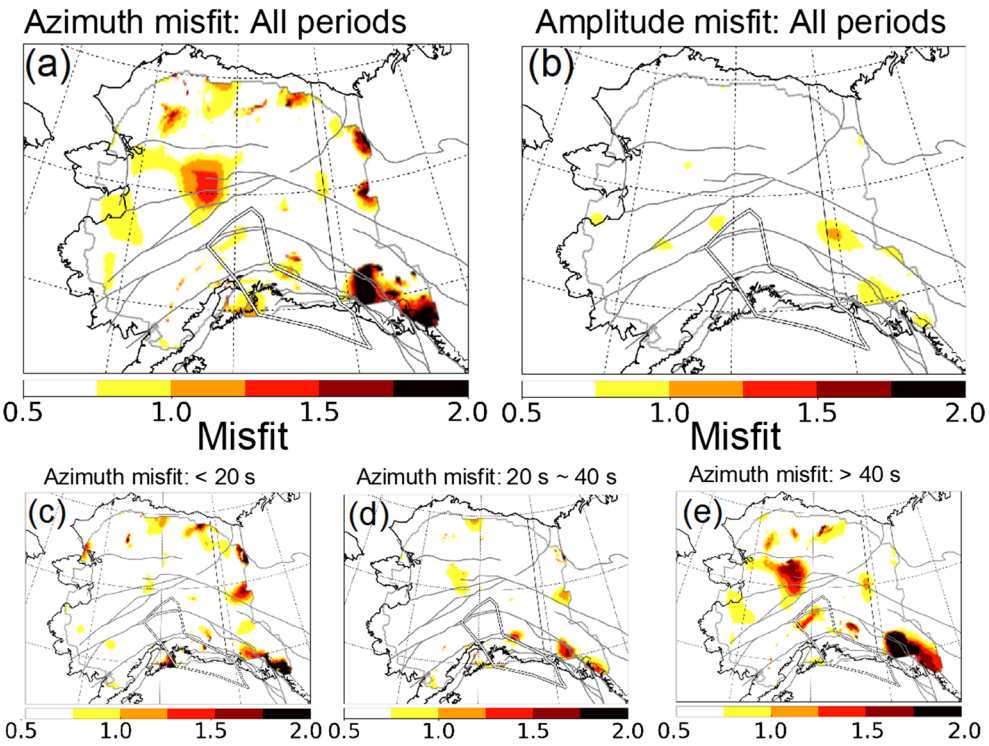

Figure 9. Misfit values (Equation 6) computed for the Two-Layer Model for fast azimuth and anisotropy amplitude. (a) Azimuthal misfit taken over all periods. (b) Amplitude misfit taken over all periods. (c) Azimuthal misfit taken only over periods <20 s. (d) Azimuthal misfit taken for intermediate periods 20 s ≤ T ≤ 40 s. (e) Azimuthal misfit taken only over periods >40 s.

azimuthal pattern, although the effect on the fast axis is more subtle. At this point, the amplitude of anisotropy with an averaging radius of 120 km is 60% larger than with the 200 km radius, which is about twice the estimate of the uncertainty in amplitude. In contrast, the change of fast axis is about 7°, which is approximately the estimate of the uncertainty in fast-axes orientation.

Figure 10b shows this difference in fast-axis orientation taken across all of Alaska at 40 s period. At the majority of locations, the fast axes are oriented within 10° of one another with the 200 and 120 km averaging radii. On average, the amplitudes are about 50% larger for an averaging radius of 120 km compared to the

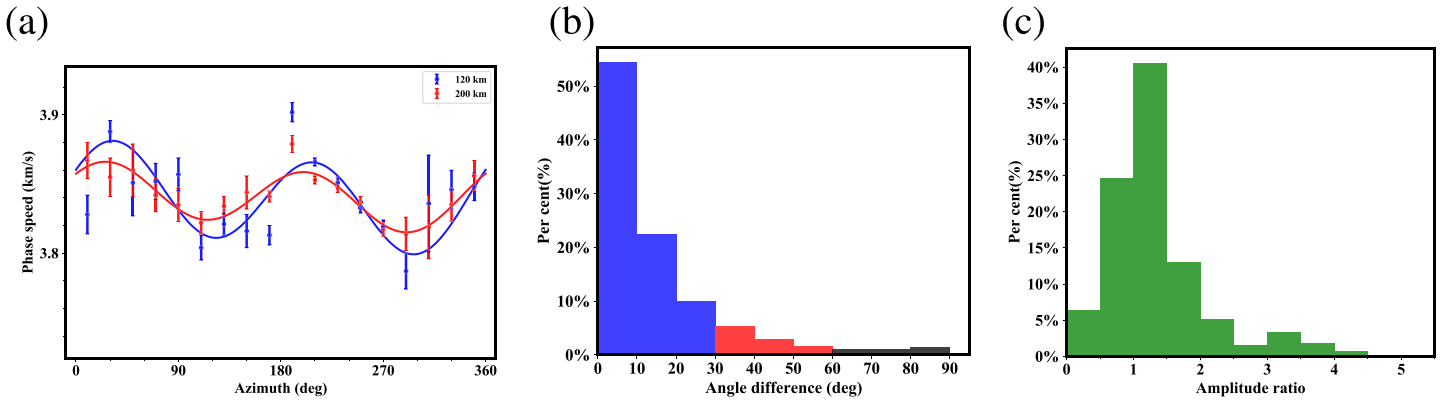

Figure 10. (a) Comparison of the azimuthal patterns of 40 s Rayleigh wave phase speeds using averaging radii of 120 km (blue bars) and 200 km (red bars). (b) Difference in the fast-axis orientations taken on a grid across Alaska between results using averaging radii of 120 and 200 km. Absolute value of the average difference is 14.5°. (c) Ratio of the amplitude of azimuthal anisotropy taken on a grid across Alaska with the 120 km result in the numerator and the 200 km result in the denominator. Mean ratio is 1.5.

200 km averaging radius. From these results we infer that the averaging radius affects the fast-axis directions less than the amplitudes, in a way that is better captured by the uncertainties that we present here. The amplitudes of azimuthal anisotropy presented in this study are affected more and may be systematically underestimated by 50% or more.

6.2. Crustal Anisotropy

The Two-Layer Model fits the short-period Rayleigh wave anisotropy information well in both fast-axis direction (Figure 9c) and amplitude (Figure 9b). But are we justified to conclude that this is the correct depth distribution of crustal azimuthal anisotropy? In a word—no. To demonstrate why, we consider candidate models in which the depth distribution of crustal azimuthal anisotropy differs from the Two-Layer Model, referred to as Alternative Models (AM) 1–3. These are as follows: (AM1) only lower crustal anisotropy from a depth of 15 km to the Moho with no anisotropy in the upper crust, (AM2) the whole crust is a single uniform layer of anisotropy from the bottom of sediments to the Moho, and (AM3) there are two independent layers of crustal anisotropy where the upper crust to 15 km and the lower crust from 15 km to Moho are allowed to have different values of φ_{SV} and A_{SV}.

We find that the misfits provided by AM1 and AM2 (maps not shown) are nearly identical to those delivered by the Two-Layer Model. In addition, although AM3 adds degrees of freedom to improve data fit, there is very little improvement in the data fit (map not shown) compared to the Two-Layer Model. Improving the fit to fast axes requires additional layer(s) in the mantle rather than in the crust, as discussed below. The similarity in misfit among these parameterizations of crustal anisotropy illustrates the intrinsic lack of depth resolution for crustal anisotropy provided by our data set.

We find, therefore, that the Two-Layer Model is consistent with the data but that upper crustal anisotropy is not necessary to fit the data. Our preference for crustal azimuthal anisotropy confined to the upper crust comes from other studies from elsewhere in the world (e.g., Feng & Ritzwoller, 2019; Lin et al., 2011; Moschetti et al., 2010; Shapiro et al., 2004; Xie et al., 2015, 2017) and the similarity between the fast-axis directions with the major fault orientations across the region of study. Indeed, by assuming the crustal material is intrinsically TI with a tilted symmetry axis, strong radial anisotropy in the middle to lower crust would imply a vertically dipping symmetry axis, which at least degrades the possibility of the existence of strong azimuthal anisotropy at the same depth ranges. We acknowledge that currently we do not have direct evidence to support our preference for confining azimuthal anisotropy in the upper crust. Thus, the existence of lower crust azimuthal anisotropy remains an open question.

As an aside, we also compare our fast-azimuth estimates for the crust with the maximum horizontal stress directions (Heidbach et al., 2016) in Figure 11. In the comparison, we discard locations where the model uncertainty in fast azimuth is greater than 30°, where the amplitude of crustal anisotropy in our model is less than 0.6% and where the quality of stress direction estimation is categorized as "D" (only keeping data points with quality of "A," "B," and "C"). We find that the Rayleigh wave fast orientations are mostly subperpendicular to the maximum horizontal stress field.

In the future, methods like those of Xie et al. (2015, 2017) to estimate the depth-dependent elastic tensor and tilt by interpreting Rayleigh wave azimuthal anisotropy simultaneously with Love wave data (radial anisotropy) may improve constraints on the depth distribution of crustal anisotropy. The tilt angle of the elastic tensor could potentially help to resolve the issue of the existence of lower crustal azimuthal anisotropy. Indeed, assuming crustal material is intrinsically TTI, a shallow tilt angle would naturally produce strong radial anisotropy and weak azimuthal anisotropy. Additionally, shear wave splitting based on local *S* phases, which reflects only crustal anisotropy, along with the stress field map may help to reveal more information about crustal azimuthal anisotropy (e.g., Crampin & Peacock, 2008).

6.3. Mantle Anisotropy

6.3.1. Data Fit

A reasonable a priori division of uppermost mantle anisotropy might include two distinct depth zones, a lithosphere, which might represent frozen-in anisotropy, and an asthenosphere in which anisotropy is controlled by present-day mantle flow (e.g., Silver, 1996; Silver & Chan, 1988; Silver & Savage, 1994). Instead, we first test whether a single mantle layer in which azimuthal anisotropy is constant from the Moho to a depth of 200 km in both fast azimuth and amplitude will allow the data to be fit. Figure 9e

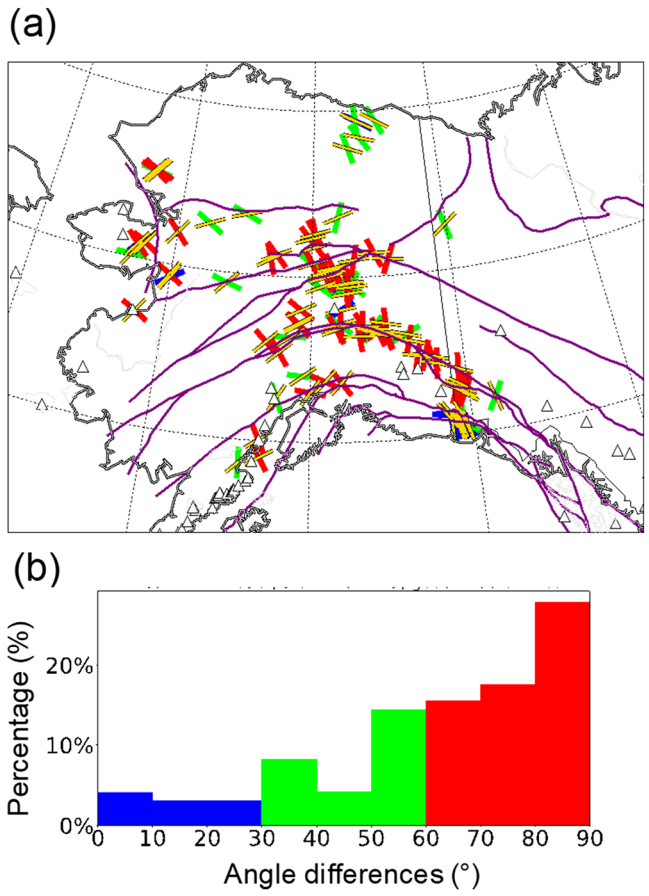

Figure 11. (a) Comparison of crustal fast directions from our model (Two-Layer Model) with maximum horizontal stress directions (Heidbach et al., 2016). The yellow bars are crustal fast directions from our model, while other colors are the maximum horizontal stress directions estimated from the stress field map: (blue bars) differences in directions are less than 30°, (green bars) differences are from 30–60°, and (red bars) differences greater than 60°. (b) Histogram of angle differences between our model and maximum horizontal stress; about 60% of locations have an angle difference larger than 60°.

shows that with one azimuthally anisotropic layer in the mantle, the Two-Layer Model, can reasonably fit long-period Rayleigh wave fast-axis observations for most of the study region. Although more layers of anisotropy could be added and the data would still be fit, when they are introduced the model tends to oscillate vertically with successive layers having fast-axis directions that are nearly perpendicular to one another. The exception lies in the Alexander and Koyukuk terranes (identified as AT and KT in Figure 1) where two layers of anisotropy are needed to fit the long-period fast-axis directions.

6.3.2. Patterns of Fast Axes in the Mantle

As indicated in Figure 8b, patterns of mantle fast axes vary regionally across Alaska and change in a way that is correlated with changes in isotropic shear wave speeds in the mantle. The large-scale high velocity isotropic anomalies occur in the compressional regions of the mantle, which include Arctic Alaska and the Pacific subduction zone. Fast directions are generally oriented approximately along the compressional direction (shown with the arrows with solid edge in Figure 8b) in each of these regions, nearly parallel to the gradient in shear wave speed. In particular, the fast directions in the slab region and back-arc areas are related to the slab geometry, being approximately slab-perpendicular in the subduction zone and then shifting to a slab-surrounding pattern in the back-arc region. Together, this transition in fast directions produces a toroidal pattern around the slab edge. This is consistent with the toroidal mantle flow directions around the Alaskan slab edge predicted by geodynamical modeling (Jadamec & Billen, 2010). The toroidal pattern is qualitatively illustrated with purple arrows in Figure 8c. In contrast, broadly speaking, the low shear speed region in the interior of Alaska undergoes tensional deformation (e.g., Redfield et al., 2007), and the fast directions are principally aligned with the directions of tensional deformation, as indicated by the dashed arrow in Figure 8b. Fast directions are more nearly perpendicular to the gradient in shear wave speed.

We also notice that the strength of anisotropy is weak at the western edge of Yakutat Terrane, and several studies (e.g., Eberhart-Phillips et al., 2006; Martin-Short et al., 2018) suggest a thicker lithosphere at this location. The sharp edge of the thick Yakutat lithosphere causes a sharp transition in fast orientation, which has been reported by SKS splitting studies (e.g., Venereau et al., 2019). This localized sharp transition in fast directions results in the apparently "weak" anisotropy in our model, because our model has a horizontal resolution of ~200 km and tends to average out the smaller scale changes.

6.3.3. Depth Extent of Anisotropy, Comparison With SKS Split Times

Our model of anisotropy is vertically homogeneous from the Moho to 200 km depth. The choice of 200 km is largely arbitrary, and we achieve a similar fit to the data with two layers of anisotropy in the upper mantle (a lithosphere and an asthenosphere) or with single layers in the mantle in which anisotropy extends only to 100 or 150 km depth. In each of the three single mantle layer cases (anisotropy extending to 100, 150, and 200 km) the fast directions are very similar, as Figure 12b illustrates. Not surprisingly, the average amplitude of anisotropy is larger for the thinner single mantle layer models (Figure 12a) than if the anisotropy extends to 200 km depth. The depth resolution of our data set is insufficient to distinguish between these alternatives, and, formally speaking, based on the surface wave data alone, we cannot determine the depth extent of anisotropy.

Nevertheless, we prefer the model in which anisotropy extends to 200 km depth. The reason is that SKS splitting is significant across much of the study region, and the splits predicted by any of the single mantle layer models are smaller by a factor of 2–3, on average, than the observed splitting, as Figure 12c shows. To produce larger *S* wave splits, our model would require larger amplitudes of anisotropy and/or the extension of

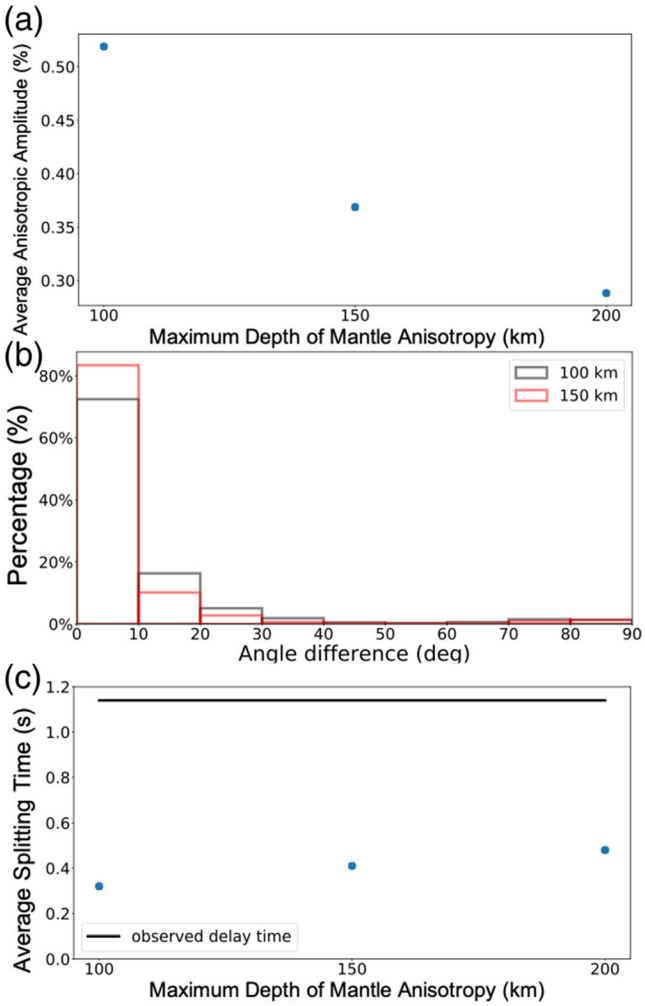

Figure 12. Varying the depth extent of anisotropy. (a) Average amplitude versus maximum depth of anisotropy. (b) A histogram showing the angle difference in fast direction relative to fast directions for anisotropy extending to 200 km if anisotropy only extended to 100 or 150 km. (c) Average *S* wave split time for models with anisotropy extending to 100, 150, and 200 km.

anisotropy to greater depths. We note, however, that the choice of the 200 km smoothing radius to aggregate data for the determination of azimuthal anisotropy may bias the amplitude of our estimates low, as discussed in section 6.1. We think it unlikely that this bias is low by a factor of 2–3, which would be what is needed to reconcile our amplitudes with those from shear wave splitting if anisotropy would extend no deeper than 200 km depth.

Figure 13c presents an amplitude comparison in a different way, showing a histogram of the predicted SKS splitting times from the mantle part of our model (in which anisotropy extends to 200 km depth) from which the observed time is subtracted. The average SKS splitting time is 1.14 s. The observed SKS splitting times are larger than the values predicted from our Two-Layer Model by an average of 0.66 s. Thus, the predicted splitting time averages about half of the observed SKS time (Venereau et al., 2019). We believe that it is likely that the fast directions we observe above 200 km in the mantle extend deeper than 200 km. The existence of significant azimuthal anisotropy beneath 200 km has also been reported in Cascadia (e.g., Mondal & Long, 2020; Wagner & Long, 2013).

6.3.4. Comparison With SKS Splitting Fast Axes

SKS splitting measurements provide an independent test of the fast-axis directions we estimate although the depth range SKS samples do not perfectly coincide with surface waves. Indeed, SKS splitting could be affected by anisotropy distributed anywhere along the ray path from the core-mantle boundary (CMB) to the surface of the Earth, although it is commonly believed that the upper mantle has the largest contribution to SKS splitting observations (e.g., Silver, 1996). The long-period Rayleigh wave data we use in this study, in contrast, are mostly sensitive to anisotropy in the uppermost mantle (e.g., Figure 7). Despite this difference in depth sensitivity, a comparison with SKS splitting provides qualitative information about the depth extent of mantle anisotropy (section 6.3.3) as well as the reliability of both data sets.

The mantle fast directions of the Two-Layer Model are consistent, on average, with SKS splitting results (Venereau et al., 2019), as shown in Figure 13. We discard data points from this comparison where the model uncertainty in fast azimuth is greater than 30° and where the amplitude of mantle anisotropy in the model is less than 0.3%. The yellow bars in Figure 13a show the orientation of fast axes of the mantle anisotropy in our model, and the blue, green, and red bars are the orientations of SKS splitting fast axes. Blue bars are locations where the differences between our model and SKS splitting observations are less than 30°, green bars where differences lie between 30° and 60°, and red bars where differences are greater than 60°. Figure 13b shows that approximately 88% of the SKS observations differ from our mantle fast directions by less than 30°.

6.3.5. On the Vertical Coherence of Deformation

The vertical homogeneity of anisotropy in the mantle part in our model is consistent with deformation that is vertically coherent, at least to the maximum depth of anisotropy recovered. Since our model extends to 200 km depth, does this mean that deformation is coherent in the mantle at least to 200 km depth? Based on surface wave data alone, no we can not refer this, because the data can be fit with anisotropy that extends to shallower or greater depths, and with anisotropy that differs between the lithosphere and the asthenosphere. However, consideration of SKS splitting data leads us to believe that anisotropy actually extends deeper than 200 km with anisotropic fast directions similar to the overlying mantle. We believe that these observations are consistent with the vertical coherence of deformation extending across much of the upper mantle except in those regions that require a second mantle layer of anisotropy: namely, the Alexander and

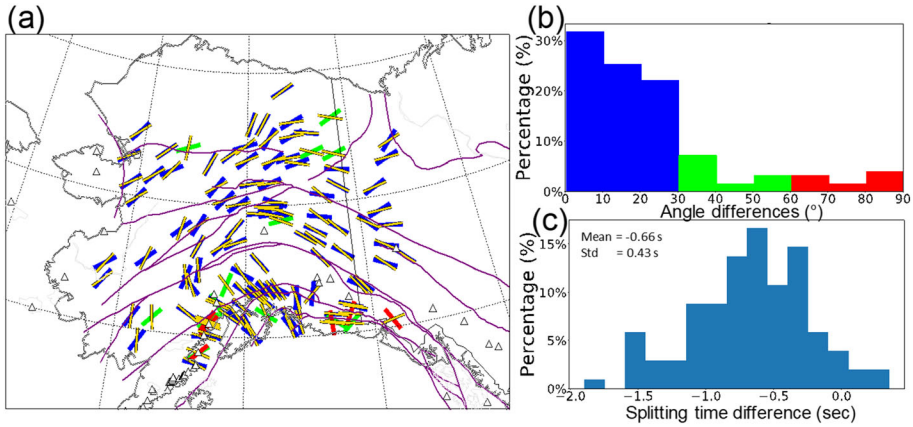

Figure 13. (a) Comparison of the fast directions in the mantle part of our model (Two-Layer Model) with those from SKS splitting (Venereau et al., 2019). The yellow bars are mantle fast directions from our model, while other colors are the fast axes estimated from SKS splitting: (blue bars) differences in fast directions are less than 30°, (green bars) differences are from 30–60°, and (red bars) differences greater than 60°. (b) Histogram of differences in fast directions between our model and SKS; about 88% of locations have an angle difference smaller than 30°. (c) Histogram of differences between predicted SKS splitting time from the mantle part of our model and the observed SKS splitting time, subtracting each observed from the predicted value. The mean and standard deviation of the differences are indicated.

Koyukuk terranes, as discussed in section 6.3.6. Again, by "vertically coherent deformation" we refer only to the mantle, as distinguished from the use of this term by Silver (1996), which refers to vertically coherent deformation in both the crust and the subcontinental mantle.

6.3.6. Regions That Require Vertical Inhomogeneity of Mantle Anisotropy and Deformation

For the Alexander and Koyukuk terranes, significant improvement in data fit is achieved by adding an independent layer below a depth of 100 km, but the fast azimuth of the upper layer is nearly perpendicular to that of the lower layer. An example of the nature of this improvement in data fit is presented in Figures 9c and 9d.

In the Alexander Terrane, the fast directions in the lower layer in the mantle are similar to the SKS splitting results. We suggest that the SKS splitting in Alexander Terrane is dominantly controlled by the lower layer, which we interpret as the asthenosphere, and deformation in the lithosphere and asthenosphere are subperpendicular to each other. In the Koyukuk Terrane, the inversion yields a fast azimuth of 87° in the upper layer and 10° in the lower one. The lower layer's fast direction is similar to the fast direction in Arctic Alaska, to the north of this point. One possibility is that the layering is caused by underthrusting of Arctic Alaska beneath the Koyukuk Terrane, but isotropic shear wave speeds in the model of Feng and Ritzwoller (2019) do not support this interpretation, partly due to the degradation of the resolution of the model at larger depths (>120 km).

Our results are consistent with the conclusion that for these two regions deformation is vertically inhomogeneous in the uppermost mantle.

Table 2
DOI of Seismic Networks Used in This Study

Network	Digital object identifier (DOI)
5C	https://doi.org/10.7914/SN/5C_2009
7C	https://doi.org/10.7914/SN/7C_2015
AK	https://doi.org/10.7914/SN/AK
AT	https://doi.org/10.7914/SN/AT
AV	https://doi.org/10.7914/SN/AV
CN	https://doi.org/10.7914/SN/CN
II	https://doi.org/10.7914/SN/II
IU	https://doi.org/10.7914/SN/IU
PN	No DOI is registered for this network.
PO	No DOI is registered for this network.
PP	No DOI is registered for this network.
TA	https://doi.org/10.7914/SN/TA
US	https://doi.org/10.7914/SN/US
XE	https://doi.org/10.7914/SN/XE_1999
XN	https://doi.org/10.7914/SN/XN_2003
XR	https://doi.org/10.7914/SN/XR_2004
XY	https://doi.org/10.7914/SN/XY_2005
XZ	https://doi.org/10.7914/SN/XZ_2005
YE	https://doi.org/10.7914/SN/YE_2007
YM	https://doi.org/10.7914/SN/YM_2002
YV	https://doi.org/10.7914/SN/YV_2006
ZE	https://doi.org/10.7914/SN/ZE_2015

7. Conclusions

We present an azimuthally anisotropic shear wave model of the crust and uppermost mantle beneath Alaska determined from surface wave dispersion. The model is represented by a two-layer parameterization of anisotropy where azimuthal anisotropy is confined to the brittle upper crust to a depth of 15 km and the uppermost mantle from the Moho to 200 km depth. This study is essentially a hypothesis test and confirms that such a model can reasonably fit the observed azimuthal variation of Rayleigh wave phase speed measurements across most of the region of study. We refer to the model we present here as the "Two-Layer Model."

The azimuthally anisotropic model derives from an inversion algorithm that is based on the first-order perturbation theory of Montagner and Nataf (1986), which relates the azimuthal variation in Rayleigh wave phase speed measurements to the azimuthal anisotropy of shear wave speeds in the Earth. The reference *V*sv model that is used to compute the sensitivity kernels is from Feng and Ritzwoller (2019).

This Two-Layer Model is able to fit the Rayleigh wave azimuthal anisotropy data across the vast majority of the region of study, except for the Alexander Terrane and Koyukuk Terrane where an additional layer in the mantle is required to fit the long-period data. A summary of our major findings and the structural features revealed by the azimuthally anisotropic model is as follows.

1. In the crust, confining azimuthal anisotropy to the brittle upper crust allows the short-period Rayleigh wave data to be fit. The resulting fast directions of the apparent crustal azimuthal anisotropy closely follow the orientation of major faults. This is consistent with crustal azimuthal anisotropy being dominantly caused by deformationally aligned cracks and fractures (e.g., Crampin, 1984) in the shallow crust. The data can be fit by allowing azimuthal anisotropy to continue into the lower crust, however.
2. For most of the region of study, the long-period Rayleigh wave data can be fit using a single azimuthally anisotropic layer in the uppermost mantle extending from the Moho to a depth of 200 km. This result is consistent with, but does not require, vertically coherent deformation in the uppermost mantle beneath Alaska and surroundings. In addition, the fast directions in the model are largely consistent with SKS splitting fast directions (Venereau et al., 2019). Because the SKS delay times predicted by our model are significantly smaller than the observed values, we suggest that anisotropy similar to the overlying mantle and vertically coherent mantle deformation extend to depths greater than 200 km across much of the region of study. However, the amplitude of azimuthal anisotropy that we infer may be biased low due to significant spatial averaging performed during the estimation.
3. The fast-axis orientations in the mantle located near the Alaska-Aleutian subduction zone describe a toroidal pattern that is consistent with mantle flow directions predicted by geodynamical modeling (Jadamec & Billen, 2010). Thus, azimuthal anisotropy in the back-arc area may be controlled by toroidal mantle flow.
4. An additional anisotropic mantle layer is required to fit the long-period Rayleigh wave observations in the Alexander Terrane and Koyukuk Terrane. The fast directions of the lower mantle layer in the Alexander Terrane are consistent with SKS splitting, producing two azimuthally anisotropic mantle layers with fast directions subperpendicular to each other.

In addition to providing information about crustal and mantle deformation and associated patterns of mantle flow in the Alaskan-Aleutian subduction zone, the models we present here may usefully serve as a starting point for further studies, such as estimating the full depth-dependent elastic tensor and tilt in the crust and mantle (e.g., Xie et al., 2015, 2017). In this context, we strive to provide reliable information about model uncertainties across the region of study, which will help guide the future use of the model.

Acknowledgments

The authors thank Eoghan Totten, two anonymous reviewers, and the Associate Editor for constructive comments that helped improve the quality of this paper. This research was supported by NSF Grant EAR-1928395 at the University of Colorado Boulder. The facilities of IRIS Data Services, and specifically the IRIS Data Management Center (https://ds.iris.edu/ds/nodes/dmc/), were used for access to waveforms, related metadata, and/or derived products used in this study. IRIS Data Services are funded through the Seismological Facilities for the Advancement of Geoscience and EarthScope (SAGE) Proposal of the National Science Foundation under Cooperative Agreement EAR-1261681. The network codes for data that are used include 5C, 7C, AK, AT, AV, CN, II, IU, PN, PO, PP, TA, US, XE, XN, XR, XY, XZ, YE, YM, YV, and ZE. The DOI numbers for the networks can be found in Table 2. This work utilized the RMACC Summit supercomputer, which is supported by the National Science Foundation (Awards ACI-1532235 and ACI-1532236), the University of Colorado Boulder, and Colorado State University. The Summit supercomputer is a joint effort of the University of Colorado Boulder and Colorado State University.

References

Babuska, V., & Cara, M. (1991). *Seismic anisotropy in the Earth* (Vol. 10). Berlin, Germany: Springer Science & Business Media. https://doi.org/10.1007/0-387-30752-4_121

Barruol, G., & Kern, H. (1996). Seismic anisotropy and shear-wave splitting in lower-crustal and upper-mantle rocks from the Ivrea zone: Experimental and calculated data. *Physics of the Earth and Planetary Interiors*, *95*(3–4), 175–194. https://doi.org/10.1016/0031-9201(95)03124-3

Behn, M. D., Hirth, G., & Kelemen, P. B. (2007). Trench-parallel anisotropy produced by foundering of arc lower crust. *Science*, *317*(5834), 108–111. https://doi.org/10.1126/science.1141269

Christensen, D. H., & Abers, G. A. (2010). Seismic anisotropy under central Alaska from SKS splitting observations. *Journal of Geophysical Research*, *115*, B04315. https://doi.org/10.1029/2009JB006712

Coney, P. J., & Jones, D. L. (1985). Accretion tectonics and crustal structure in Alaska. *Tectonophysics*, *119*(1–4), 265–283. https://doi.org/10.1016/0040-1951(85)90042-3

Crampin, S. (1984). Effective anisotropic elastic constants for wave propagation through cracked solids. *Geophysical Journal International*, *76*(1), 135–145. https://doi.org/10.1111/j.1365-246X.1984.tb05029.x

Crampin, S., & Peacock, S. (2008). A review of the current understanding of seismic shear-wave splitting in the Earth's crust and common fallacies in interpretation. *Wave Motion*, *45*(6), 675–722. https://doi.org/10.1016/j.wavemoti.2008.01.003

Eberhart-Phillips, D., Christensen, D. H., Brocher, T. M., Hansen, R., Ruppert, N. A., Haeussler, P. J., & Abers, G. A. (2006). Imaging the transition from Aleutian subduction to Yakutat collision in central Alaska, with local earthquakes and active source data. *Journal of Geophysical Research*, *111*, 1–31. https://doi.org/10.1029/2005JB004240

Faccenda, M., Burlini, L., Gerya, T. V., & Mainprice, D. (2008). Fault-induced seismic anisotropy by hydration in subducting oceanic plates. *Nature*, *455*(7216), 1097–1100. https://doi.org/10.1038/nature07376

Feng, L., & Ritzwoller, M. H. (2019). A 3-D shear velocity model of the crust and uppermost mantle beneath Alaska including apparent radial anisotropy. *Journal of Geophysical Research: Solid Earth*, *124*, 10,468–10,497. https://doi.org/10.1029/2019JB018122

Freymueller, J. T., Woodard, H., Cohen, S. C., Cross, R., Elliott, J., Larsen, C. F., et al. (2008). Active deformation processes in Alaska, based on 15 years of GPS measurements. *Active tectonics and seismic potential of Alaska*, *179*, 1–42. https://doi.org/10.1029/179GM02

Gou, T., Zhao, D., Huang, Z., & Wang, L. (2019). Aseismic deep slab and mantle flow beneath Alaska: Insight from anisotropic tomography. *Journal of Geophysical Research: Solid Earth*, *124*, 1700–1724. https://doi.org/10.1029/2018JB016639

Hacker, B. R., Ritzwoller, M. H., & Xie, J. (2014). Central Tibet has a partially melted, mica-bearing crust. *Tectonics*, *33*, 1408–1424. https://doi.org/10.1002/2014TC003534

Hanna, J., & Long, M. D. (2012). SKS splitting beneath Alaska: Regional variability and implications for subduction processes at a slab edge. *Tectonophysics*, *530*, 272–285. https://doi.org/10.1016/j.tecto.2012.01.003

Heidbach, O., Rajabi, M., Reiter, K., Ziegler, M., & the WSM Team (2016). World stress map database release 2016, GFZ data services, http://doi.org/10.5880/WSM.2016.001

Herrmann, R. B. (2013). Computer programs in seismology: An evolving tool for instruction and research. *Seismological Research Letters*, *84*, 1081–1088. https://doi.org/10.1785/0220110096

Jadamec, M. A., & Billen, M. I. (2010). Reconciling surface plate motions with rapid three-dimensional mantle flow around a slab edge. *Nature*, *465*(7296), 338–341. https://doi.org/10.1038/nature09053

Jiang, C., Schmandt, B., Ward, K. M., Lin, F. C., & Worthington, L. L. (2018). Upper mantle seismic structure of Alaska from Rayleigh and *S* wave tomography. *Geophysical Research Letters*, *45*, 10–350. https://doi.org/10.1029/2018GL079406

Johnston, S. T. (2001). The Great Alaskan Terrane Wreck: Reconciliation of paleomagnetic and geological data in the northern Cordillera. *Earth and Planetary Science Letters*, *193*(3–4), 259–272. https://doi.org/10.1016/S0012-821X(01)00516-7

Lin, F. C., & Ritzwoller, M. H. (2011). Apparent anisotropy in inhomogeneous isotropic media. *Geophysical Journal International*, *186*(3), 1205–1219. https://doi.org/10.1111/j.1365-246X.2011.05100.x

Lin, F. C., Ritzwoller, M. H., & Snieder, R. (2009). Eikonal tomography: Surface wave tomography by phase front tracking across a regional broad-band seismic array. *Geophysical Journal International*, *177*(3), 1091–1110. https://doi.org/10.1111/j.1365-246X.2009.04105.x

Lin, F. C., Ritzwoller, M. H., Yang, Y., Moschetti, M. P., & Fouch, M. J. (2011). Complex and variable crustal and uppermost mantle seismic anisotropy in the western United States. *Nature Geoscience*, *4*(1), 55–61. https://doi.org/10.1038/ngeo1036

Long, M. D. (2013). Constraints on subduction geodynamics from seismic anisotropy. *Reviews of Geophysics*, *51*, 76–112. https://doi.org/10.1002/rog.20008

Long, M. D., & Silver, P. G. (2008). The subduction zone flow field from seismic anisotropy: A global view. *Science*, *319*(5861), 315–318. https://doi.org/10.1126/science.1150809

Long, M. D., & van der Hilst, R. D. (2006). Shear wave splitting from local events beneath the Ryukyu arc: Trench-parallel anisotropy in the mantle wedge. *Physics of the Earth and Planetary Interiors*, *155*(3–4), 300–312. https://doi.org/10.1016/j.pepi.2006.01.003

Martin-Short, R., Allen, R., Bastow, I. D., Porritt, R. W., & Miller, M. S. (2018). Seismic imaging of the Alaska subduction zone: Implications for slab geometry and volcanism. *Geochemistry, Geophysics, Geosystems*, *19*, 4541–4560. https://doi.org/10.1029/2018GC007962

Mondal, P., & Long, M. D. (2020). Strong seismic anisotropy in the deep upper mantle beneath the Cascadia backarc: Constraints from probabilistic finite-frequency SKS splitting intensity tomography. *Earth and Planetary Science Letters*, *539*, 116172. https://doi.org/10.1016/j.epsl.2020.116172

Montagner, J. P., & Nataf, H. C. (1986). A simple method for inverting the azimuthal anisotropy of surface waves. *Journal of Geophysical Research*, *91*(B1), 511–520. https://doi.org/10.1029/JB091iB01p00511

Moore, T. E., & Box, S. E. (2016). Age, distribution and style of deformation in Alaska north of 60°N: Implications for assembly of Alaska. *Tectonophysics*, *691*, 133–170. https://doi.org/10.1016/j.tecto.2016.06.025

Moschetti, M. P., Ritzwoller, M. H., Lin, F., & Yang, Y. (2010). Seismic evidence for widespread western-US deep-crustal deformation caused by extension. *Nature*, *464*(7290), 885–889. https://doi.org/10.1038/nature08951

Petrescu, L., Darbyshire, F., Bastow, I., Totten, E., & Gilligan, A. (2017). Seismic anisotropy of Precambrian lithosphere: Insights from Rayleigh wave tomography of the eastern Superior Craton. *Journal of Geophysical Research: Solid Earth*, *122*, 3754–3775. https://doi.org/10.1002/2016JB013599

Redfield, T. F., Scholl, D. W., Fitzgerald, P. G., & Beck, M. E. Jr. (2007). Escape tectonics and the extrusion of Alaska: Past, present, and future. *Geology*, *35*(11), 1039–1042. https://doi.org/10.1130/G23799A.1

Savage, M. K. (1999). Seismic anisotropy and mantle deformation: What have we learned from shear wave splitting? *Reviews of Geophysics*, *37*(1), 65–106. https://doi.org/10.1029/98RG02075

Savage, M. K., Silver, P. G., & Meyer, R. P. (1990). Observations of teleseismic shear-wave splitting in the Basin and Range from portable and permanent stations. *Geophysical Research Letters*, *17*(1), 21–24. https://doi.org/10.1029/GL017i001p00021

Shapiro, N. M., Ritzwoller, M. H., Molnar, P., & Levin, V. (2004). Thinning and flow of Tibetan crust constrained by seismic anisotropy. *Science*, *305*(5681), 233–236. https://doi.org/10.1126/science.1098276

Silver, P. G. (1996). Seismic anisotropy beneath the continents: Probing the depths of geology. *Annual Review of Earth and Planetary Sciences*, *24*(1), 385–432. https://doi.org/10.1146/annurev.earth.24.1.385

Silver, P. G., & Chan, W. W. (1988). Implications for continental structure and evolution from seismic anisotropy. *Nature*, *335*(6185), 34–39. https://doi.org/10.1038/335034a0

Silver, P. G., & Savage, M. K. (1994). The interpretation of shear-wave splitting parameters in the presence of two anisotropic layers. *Geophysical Journal International*, *119*(3), 949–963. https://doi.org/10.1111/j.1365-246X.1994.tb04027.x

Smith, M. L., & Dahlen, F. A. (1973). The azimuthal dependence of love and Rayleigh wave propagation in a slightly anisotropic medium. *Journal of Geophysical Research*, *78*(17), 3321–3333. https://doi.org/10.1029/JB078i017p03321

Tarantola, A. (2005). Inverse problem theory and methods for model parameter estimation (Vol. 89). Society of Industrial and Applied Mathematics. https://doi.org/10.1137/1.9780898717921

Venereau, C. M., Martin-Short, R., Bastow, I. D., Allen, R. M., & Kounoudis, R. (2019). The role of variable slab dip in driving mantle flow at the eastern edge of the Alaskan subduction margin: Insights from shear-wave splitting. *Geochemistry, Geophysics, Geosystems*, *20*, 2433–2448. https://doi.org/10.1029/2018GC008170

Vinnik, L. P., Makeyeva, L. I., Milev, A., & Usenko, A. Y. (1992). Global patterns of azimuthal anisotropy and deformations in the continental mantle. *Geophysical Journal International*, *111*(3), 433–447. https://doi.org/10.1111/j.1365-246X.1992.tb02102.x

Wagner, L. S., & Long, M. D. (2013). Distinctive upper mantle anisotropy beneath the High Lava Plains and Eastern Snake River Plain, Pacific northwest, USA. *Geochemistry, Geophysics, Geosystems*, *14*, 4647–4666. https://doi.org/10.1002/ggge.20275

Wang, Y., & Tape, C. (2014). Seismic velocity structure and anisotropy of the Alaska subduction zone based on surface wave tomography. *Journal of Geophysical Research: Solid Earth*, *119*, 8845–8865. https://doi.org/10.1002/2014JB011438

Ward, K. M., & Lin, F. C. (2018). Lithospheric structure across the Alaskan cordillera from the joint inversion of surface waves and receiver functions. *Journal of Geophysical Research: Solid Earth*, *123*, 8780–8797. https://doi.org/10.1029/2018JB015967

Wiemer, S., Tytgat, G., Wyss, M., & Duenkel, U. (1999). Evidence for shear-wave anisotropy in the mantle wedge beneath south central Alaska. *Bulletin of the Seismological Society of America*, *89*(5), 1313–1322.

Xie, J., Ritzwoller, M. H., Brownlee, S. J., & Hacker, B. R. (2015). Inferring the oriented elastic tensor from surface wave observations: Preliminary application across the western United States. *Geophysical Journal International*, *201*, 996–1021. https://doi.org/10.1093/gji/ggv054

Xie, J., Ritzwoller, M. H., Shen, W., & Wang, W. (2017). Crustal anisotropy across eastern Tibet and surroundings modeled as a depth-dependent tilted hexagonally symmetric medium. *Geophysical Journal International*, *209*, 466–491. https://doi.org/10.1093/gji/ggx004

Yang, X., Fischer, K. M., & Abers, G. A. (1995). Seismic anisotropy beneath the Shumagin Islands segment of the Aleutian-Alaska subduction zone. *Journal of Geophysical Research*, *100*(B9), 18,165–18,177. https://doi.org/10.1029/95JB01425

Yao, H., Van Der Hilst, R. D., & Montagner, J. P. (2010). Heterogeneity and anisotropy of the lithosphere of SE Tibet from surface wave array tomography. *Journal of Geophysical Research*, *115*, B12307. https://doi.org/10.1029/2009JB007142